Mid-Period Rayleigh Wave Attenuation Model for Asia

Anatoli L. Levshin[1], Xiaoning Yang[2], Mikhail P. Barmin[1],
and Michael H. Ritzwoller[1]

University of Colorado at Boulder[1], Los Alamos National Laboratory[2]

SUMMARY

We present an attenuation model for mid-period Rayleigh waves in Central Asia and surrounding regions. This model is defined by maps of attenuation coefficient across the region of study in the period band 14-24 s. The model is constructed to characterize the regional variations in attenuation of seismic waves in the crust, which are related to the tectonic history of the studied territory, to calibrate the regional surface-wave magnitude scale and to extend the teleseismic 'surface-wave magnitude – body-wave magnitude' (*Ms-mb*) discriminant to regional distances. The construction of the model proceeds in three stages: (1) data accumulation and amplitude measurements, (2) estimation of the integral of attenuation coefficients along sources-station paths, or between two stations, and (3) tomographic inversion of the attenuation data.

The first stage in model construction is the measurement of Rayleigh wave spectral amplitudes. We collected and processed waveform data for 200 earthquakes occurring throughout 2003-2006 inside and around Eurasia. The records of about 135 broadband permanent and temporary stations were used. The existing broadband station distribution and the pattern of seismicity provided sufficient number of spectral amplitude measurements between 14 and 24 s periods for the construction of the two–dimensional (2-D) tomographic maps of attenuation coefficients. Measurements at periods below about 14 s are too scarce or too scattered for tomographic inversion.

 At the second stage of the work, the integral of attenuation coefficients along given paths are estimated using both inter-station measurements and single-station measurements corrected for source and receiver terms. The corrections are based on a three-dimensional (3-D) global model of the crust and upper mantle CUB2.0 by Shapiro and Ritzwoller (2002). .

The third stage includes the refining of source parameters (especially the depth and the scalar moments), recalculation of attenuation-coefficient integrals after this refinement, grooming of resulting coefficients, and the multi-stage tomograhic inversion of the data. As a result, tomographic maps of attenuation for the set of periods from 14 to 24 s are obtained. The tomographic maps for this range of periods have been obtained which exhibit clear correlation with geology and tectonics of the territory under study.

1. Introduction

Knowledge of the losses of seismic energy during the propagation of the wave from the source to the receivers is essential for the understanding of the tectonic history of the region under study, and the estimation of the surface-wave magnitude *Ms* and the seismic moment of the source. This is especially important for the monitoring of underground nuclear explosions, in which the estimation of *Ms* is used as a part of the most robust seismic discriminant, the *Ms-mb* discriminant. In order to apply this discriminant to regional-distance monitoring, a modified *Ms* formula using shorter-period (< 20 s) surface wave amplitudes is required (e.g., Keilis-Borok, 1960; Marshall and Basham, 1972; Bonner et al., 2006; Russell, 2006). At shorter periods the lateral variation of the surface-wave attenuation becomes an even more important factor in causing the station magnitude scatter. The two-dimensional (2-D), mid-period (14-24 s)

surface-wave attenuation model that we develop in this study not only improves our knowledge of the tectonic history of the region, but also can be used to implement 2-D path corrections in calculating regional short-period *Ms* to reduce station-magnitude scatter.

The first stage in the model construction is the measurement of Rayleigh-wave spectral amplitudes. To overcome inherent difficulties due to multipathing and scattering of short-period surface waves we applied the Surface Wave Amplitude Measurement Tool (SWAMTOOL) designed at the Los Alamos National Laboratory (LANL) (Yang et al., 2005). We enhanced SWAMTOOL by providing different options for phase-matched filtering of surface wave signals (Levshin et al., 2006). Waveform data for 200 earthquakes occurring throughout 2003-2006 inside and around Eurasia from about 135 broadband permanent and temporary stations have been collected and processed. This data set provided a sufficient number of spectral amplitude measurements between 14 and 24 s periods for the construction of the 2-D tomographic maps of attenuation coefficients.

At the second stage of the work, the integrals of attenuation coefficients along source-station paths, or between two stations are estimated using both single-station and inter-station measurements corrected for the source and receiver terms. The corrections are based on a 3-D global model of the crust and upper mantle (CUB2.0) of Shapiro and Ritzwoller (2002). Information about source mechanisms of selected events is taken from the CMT catalog (Dziewonski et al., 1981) and the hypocenter information is from EHB catalog by Engdahl et al., 1998).

The third stage includes the refining of source parameters (especially the depth and the scalar moments), recalculation of the attenuation-coefficient integrals after this refinement, grooming of resulting coefficients, and the multi-stage tomograhic inversion of the data. As a result, tomographic maps of attenuation coefficients for the set of periods from 14 to 24 s are obtained. This work complements numerous studies of surface wave attenuation in Asia carried out by Cong & Mitchell (1998, 1998a), Mitchell et al. (1998), Jemberie & Mitchell (2004, 2005), Stevens et al. (2001), Stevens et al. (2007), Taylor et al. (2003), Yang et al. (2004) and others.

2. Surface- Wave Attenuation in Laterally Inhomogeneous Media: Elements of Theory

We assume that the Rayleigh wave propagates in a laterally and radially inhomogeneous medium, in which elastic and anelastic parameters change smoothly along the Earth's surface. The term "smoothly" means that the changes of these parameters (wave speed, density, thickness of layers, Q_s) along the distance of a wavelength are small. Surface waves are generated by a point source with a moment tensor **M**. The tensor and coordinates of the source including depth h are presumed to be known. Following the asymptotic ray theory of surface wave propagation in a 3-D medium (Woodhouse, 1974; Levshin, 1985; Levshin et al., 1989) we define the spectral amplitude $A(\omega)$ for a given event-station pair as

$$A(\omega, \Delta, \varphi) = S(\omega, h, \varphi) P(\omega, \Delta) B(\omega). \qquad (1)$$

Here ω is the circular frequency in rad/s, φ is the azimuth from epicenter to station, and Δ is the epicentral distance in degrees. The source term $S(\omega, h, \varphi)$ may be presented as

$$S(\omega, h, \varphi) = M_0 \mid M_{ij} E^{ij}(\omega, h, \varphi) \mid, \quad i,j=1,2,3 \qquad (2)$$

Here M_0 is the scalar moment, M_{ik} are the components of the normalized moment tensor, and $E^{ij}(\omega,h,\varphi)$ are components of the strain tensor for the Rayleigh wave at the given frequency and depth, which depends on the one-dimensional (1-D) structure around the epicenter. The propagation term P is defined by the elastic and anelastic structure between the source and receiver. Assuming that the wave propagates along the great circle L between the source and the receiver, we have

$$\boxed{\times} \; P(\omega,\Delta) = \frac{\exp(-\omega \int_L \frac{dl}{2U_R(\omega,l)Q_R(\omega,l)})}{\sqrt{r_o \sin\Delta}} = \frac{\exp(-\int_L \gamma_R(\omega,l)dl)}{\sqrt{r_o \sin\Delta}}, \boxed{\times}\boxed{\times} \qquad (3)$$

where r_0 is the Earth's radius. Integrals $I = \int_L \gamma_R(\omega,l)dl$ and $\Delta = \int_L dl$ are taken along the great circle through the source and receiver. Factors U_R, Q_R, γ_R are group velocity, quality factor Q, attenuation coefficient of Rayleigh wave respectively. All these factors depend on frequency ω and correspond to 1-D radially-inhomogeneous local structure at the point l on the great circle. This structure is described by functions $a(r), b(r), \rho(r), Q_P(r), Q_S(r)$, where a and b are velocities of P and S waves, ρ is density, Q_P, Q_S are intrinsic Q factors for P and S waves, all of which depending on the distance r from the Earth's center. The receiver term $B(\omega)$ depends on the structure near the receiver:

$$B(\omega) = \left(I_{0R}(\omega)U_R(\omega)k_R(\omega)\right)^{-\frac{1}{2}}. \qquad (4)$$

Here $I_{0R}(\omega)$ is the normalized kinetic energy, $k_R(\omega)$ and $U_R(\omega)$ are the wavenumber and group velocity of the Rayleigh wave at the given frequency ω for the 1-D local model under the station. Similar expressions are valid for Love wave.

Our goal is to predict the value of the integral $I(\omega)$ between any two points inside the region under study for prescribed range of periods $T=2\pi/\omega$. This will be done by comparing the observed amplitude spectrum $A_{obs}(\omega)$ for each event-station pair with predicted spectrum from an elastic model for this pair:

$$A_{pred}(\omega) = S(\omega,h,\varphi)\frac{1}{\sqrt{r_0 \sin\Delta}} B(\omega) \, . \qquad (5)$$

The ratio of predicted and observed amplitude spectra is used to find the integral I:

$$\boxed{\times} . \qquad (6)$$

In the case when we have two stations that are at approximately the same azimuth φ from the source, it is possible to use the ratio of the two observed spectra $A_{obs1}(\omega)$ and $A_{obs2}(\omega)$ to find the integral I_{12}:

$$I_{12} = \int_{L_{12}} \gamma_R(\omega,l)dl = \ln\left[\frac{A_{obs1}B_2\sqrt{\sin\Delta_1}}{A_{obs2}B_1\sqrt{\sin\Delta_2}}\right] \qquad (7)$$

between the two stations. Here L_{12} is the path along the great circle between the two stations.

Interpreting amplitude spectra measurements
The transition from amplitude spectra to attenuation coefficients for the source to receiver paths is based on information about the source mechanism and depth, which is originally taken from

the CMT catalog (Dziewonski et al., 1981). Uncertainties in CMT solutions for the best double couple orientation and source depth have a strong influence on the attenuation coefficients. We illustrate this by simulating the effects of uncertainties in source mechanism, when strike, dip, and slip of the best couple are varied by +/- 5 degrees (Figure 1, left). The simulation is performed for a realistic crustal model and source parameters. Variations in the amplitude spectrum are on the order of 10%. More dramatic effects are produced by the uncertainty in the source depth (Figure 1, right). The maximum uncertainty in the spectrum occurs when the source excitation function experiences a minimum at or near the source depth. Although the details will depend on source mechanism and local structure, this simulation shows that a 5 km error in source may produce up to a 50% error in the spectral measurements at periods between 10 s and 20 s. If the event depth is known to lie between 15 and 25 km, the amplitude spectra are expected to be similar between 10- and 20- s period. Spectra in this period range are very sensitive to the depth of shallower events. Inter-station measurements are significantly less sensitive to these factors, but the number of these measurements is much lower than the number of source/receiver measurements (Figure 3b).

Effects of lateral inhomogeneities
Uncertainties in knowledge of the local structure of the crust near the source and receiver may also distort the estimated attenuation coefficients. This could happen due to significant differences in the crustal structure near the source and receiver locations (single-station case) or near the location of the receivers (inter-station case).

A simulated example is shown in Figure 2 for dramatically different crustal structures at the source and receiver. This effect is not as severe as the effect of uncertainty in source depth. In addition, this effect can be ameliorated in the transition from amplitude spectra to attenuation coefficients by using a realistic 3-D model of the Eurasian crust (e.g., Shapiro & Ritzwoller, 2002). Effects of focusing and defocusing of the surface wave in a laterally inhomogeneous crust unaccounted in (5) and (7) may significantly contribute to the data scatter.

3. Data Acquisition and Processing

Surface wave data acquisition
We collected surface-wave waveform data for 200 events that occurred in and around Eurasia through 2003-2006 (Table 1, electronic supplement). Selected events are characterized by magnitudes M_s between 5 and 6 and source depths of less than 70 km. Several global and regional broadband networks have existed in Eurasia during the considered time interval. These include Global Seismographic Network (GSN), International Monitoring System (IMS), GEOSCOPE, GEOFON, Mediterranean Seismic Network (MEDNET), China Digital Seismological Network (CDSN), Kyrgyz Seismic Network (KNET), Kazakhstan Seismic Network (KAZNET), and others. The list of 135 stations used in this study and their coordinates is provided in Table 2 (electronic supplement). Maps with the station and event distribution are shown in Figure 3a. The original seismogram records were requested and provided by the Data Management Center (DMC) of Incorporated Research Institutions for Seismology (IRIS). The criteria for selecting station pairs are: (a) the difference in azimuths from the epicenter to the stations is less than 1° and (b) the distance between the stations is more than 300 km and less than 5000 km. Figure 3b presents the number of obtained single-station and inter-station measurements as a function of period. Altogether more than 9000 records from 135 seismic stations were selected for measurements. The moment-tensor

solutions of selected events are taken from the CMT catalog (Dziewonski et al., 1981) and the hypocenter information is from the catalog EHB by Engdahl et al. (1998).

Measurements of amplitude spectra

Following standard data-preprocessing procedure, all records were corrected for the instrument response and converted to ground displacement using the Seismic Analysis Code (SAC). Inherent difficulties in the measurement of surface wave amplitude spectra result from multipathing and scattering of short-period surface waves crossing strong lateral inhomogeneities in the crust. To overcome these difficulties we apply SWAMTOOL designed at the LANL (Yang et al., 2005), which incorporates dispersion analysis, phase-matched filtering, and additional means to reduce the contamination of surface-wave amplitudes by various noise sources and to estimate the quality and reliability of measurements. We have enhanced SWAMTOOL by providing improved options for phase-matched filtering of the surface-wave signals (Levshin et al., 2006). As the output, we obtain the raw spectral amplitudes of Rayleigh waves in the period range dictated by the magnitude of the earthquake, the epicentral distance, and the level of the background noise. We compare amplitude spectra obtained by SWAMTOOL with independent measurements of the same records by means of the Frequency-Time Analysis (FTAN) (Levshin et al., 1972; Levshin et al., 1989; Ritzwoller and Levshin, 1998). The similarity of the results from SWAMTOOL and FTAN as well as numerous repeatability tests (see Figures 4 and 5) confirms the validity of the measurements.

Data selection

The spectral amplitudes at designated periods were corrected according to equations (6) and (8) above. The correction was based on the 3-D global model of the crust and upper mantle CUB2.0 by Shapiro and Ritzwoller (2002). This model is constructed on a 2°×2° grid. To find factors $S(\omega,h,\varphi)$ for given moment tensor $M_0\boldsymbol{M}$ and depth h, we calculate the strain $\mathbf{E}(\omega,h,\varphi)$ for the 1-D structure at the grid node nearest to the epicenter. To avoid effects caused by the near-nodal radiation, we exclude records for which the theoretical value of $|M_{ij}E^{ij}|$ for a given azimuth φ is less than 0.1 of its maximum value. To calculate factor $B(\omega)$ according to equation (4), we use the 1-D structure at the grid node nearest to the station. The local values of $B(\omega)$ differ from the average across the region in the range of ± 10% , except deep seas and oceans. Spectral attenuation coefficients are estimated using both single-station measurements corrected for the source and receiver terms and inter-station measurements. The corrected amplitudes for 18 s period are plotted as a function of distance in Figure 6. The figure shows that there are indications of a possible bias in source parameters, which results in non-zero crossing by the least-square line at the zero distance. Moreover, many calculated average attenuation coefficients are negative, especially at epicentral distances less than 5000 km, in contradiction of the physical nature of attenuation. There are several possible explanations for this phenomenon:

    (1) errors in stations' amplitude responses;

    (2) contamination of the measured spectra of the fundamental-mode Rayleigh wave by higher modes and multiple arrivals;

    (3) errors in source parameters (the source depth, moment tensor, scalar moment);

    (4) inadequate description of wave propagation by the ray theory (neglecting off-path propagation, scattering, etc.).

The maximum number of negative average attenuation coefficients in raw data occurs at short distances (10-12 % of all measurements). This percentage decreases at least in two times at greater epicentral distances. To overcome this effect we introduced the procedures for declustering and weighting of data depending on the epicentral distance. Declustering procedure selects data belonging to similar paths, finds the average amplitude for the cluster

and rejects data, of which the deviation from the average value is more than the Root mean square (*Rms)* value of deviations. Further grooming of the data has been done after obtaining the preliminary tomographic maps of $\gamma(\omega)$ by excluding paths to 6 stations which generated anomalously large residuals. Such stations are mainly deployed on islands or very close to the ocean coast and very sensitive to station-epicenter azimuths. The numbers of paths before and after this procedure for both epicenter-station and inter-station measurements are shown in Figure 3b. The resulting path density of the data used in the tomographic inversion is shown in Figure 7. The path density is defined as the number of paths crossing a 2°×2° equatorial cell.

4. Attenuation-Coefficient Tomography

Tomographic inversion
To invert selected measurements for tomographic maps, we applied, with some modifications, the inversion algorithm described by Barmin et al., 2001. As was shown by Yang et al. (2004), and Levshin et al. (2006), CMT moment tensor solutions may be biased with a tendency to exaggerate the scalar moment M_o for Asia earthquakes. Such a bias may distort our measurements of attenuation coefficients. To avoid these distortions, we modified our algorithm of inversion by introducing an additional unknown δM_{0j} in the functional *F(T)* designed for the minimization of the difference between predicted and observed decay of surface-wave amplitudes along selected paths.

Let us consider residual d_{ij} of the measurement at given period T along the *ij*-th path from the *j*-th epicenter to the *i*-th station as

$$d_{ij} = q_{ij}^{\,obs} - q_{ij}^{\,o} = \int_{ij} m(\mathbf{r})ds + \ln(\delta M_{0j}). \tag{8}$$

Here $q_{ij}^{\,obs}$ is the value of the integral I_{ij} found from observations for the *ij*-path and $q_{ij}^{\,o}$ is the value of the same integral predicted by the map to be inverted. Function $m(\mathbf{r})$ is the perturbation of the model from the reference model $m_0(\mathbf{r})$. The functional for minimization is defined as

$$F(T) = \tfrac{1}{N} \sum_{ij} (w_{ij} d_{ij})^2. \tag{9}$$

We assume that

$$m_0(\mathbf{r}) = const = \frac{1}{N} \sum_{i,j} \frac{q_{ij}^{\,obs}}{\Delta_{ij}} \;,\; \boxed{\text{X}} \tag{10}$$

where N is the total number of paths and Δ_{ij} is the length of the *ij*-path. The weighting in (10) is done by applying

$$w_{ij} = \frac{0.5(\Delta_{ij} + \Delta_{max}) - \Delta_{min}}{\Delta_{max} - \Delta_{min}}. \tag{11}$$

Here w_{ij} is the weight applied to corrected amplitudes; Δ_{max} and Δ_{min} are maximum and minimum epicentral distances of the data at given period, respectively.
The tomographic inversion proceeds in two steps.
    At the first step the initial model $m_0(\mathbf{r})$ is taken to be a spatially-homogeneous model obtained by averaging observed values $q_{ij}^{\,obs}$ for a given period. We minimize *F(T)* using several damping parameters described in Barmin et al. (2001) with an additional damping parameter for the scalar-moment correction. Numerous experiments with different values of damping parameters provided the optimal procedure for inversion. This procedure was applied to data for

a set of periods between 14 and 24 s. How much the corrected scalar moments differ from CMT moments is shown in Figure 8. One can see the tendency for M_0 to decrease in order to fit the data. The same tendency was noticed by Yang et al. (2004).

For the second step of tomographic inversion we selected period T=18 s as a representative period for estimation of M_{0j} and used source corrections obtained for 18-s data to calculate predicted amplitudes at all periods before inversion. The starting models were still spatially-homogeneous ones found by a new averaging of corrected q_{ij}^{obs}.

Resulting tomographic maps of attenuation coefficients γ_R for Asia and surrounding regions are shown in Figure 9. These maps display many features that correlate well with the geology and tectonics of the studied region. Low attenuation is typical in stable regions such as East Europe and the Siberian Platforms, the Indian Shield, the Arabian platform, the Yangtze craton, and others. High attenuation is observed in tectonically active regions such as the Himalayas, the Tien-Shan, the Pamir, the Zagros, and etc. Within the period range from 14 to 24 s, the overall attenuation decreases as the period increases. The spatial resolution varies across the continental part of maps from 180 to 400 km. In general, there is a good agreement between our 20-s map (Figure 9) and the 20-s map of Yang et al. (2004), which were based on a different set of input data.

5. Evaluating the Attenuation Models

We estimate the variance reduction which was achieved with our tomographic maps by comparison of their residual statistics with ones found for spatially homogeneous models. For periods between 14 and 24 s, variance reduction is between 30 and 40 % (Figure 10a). Fixing the scalar moment for the whole set of periods using the results for 18 s did not significantly degrade the data fit. Tomographic maps obtained from inversions with the scalar-moment correction included as an unknown are very similar to the maps shown in Figure 9.

We also used inter-station amplitude measurements, which are less subjected to the uncertainty in source parameters, to validate the inverted maps. We traced inter-station paths through the inverted maps and calculated integrals I_{12} from (8). Figure 10b demonstrates the resulting variance reductions for inter-station paths in comparison with ones achieved for epicenter-station paths. Differences between the values of this integral predicted by the maps and observed ones were used to calculate standard deviations for a set of periods. From Figure 11a one can see that *Rms* of residuals for inter-station measurements are about 1.5 times smaller than for epicenter-station measurements. All this confirms that our corrections of the scalar moments did not distort the tomographic maps.

6. Discussion

We mentioned earlier that the amplitude measurements are characterized by a strong scatter, and some of them produce negative values of attenuation coefficients. To understand possible factors contributing to these phenomena, we analyzed residuals d_{ij} obtained after the last tomographic inversion for each selected period. We compare average *Rms* values of residuals for all paths and subsets of selected paths. Here is what we found:
1) Paths ending at a given station. We observe significant increase in *Rms* relative to the average values only for paths to few stations situated near the ocean and deep-sea coasts (e.g., station DVA in Philippines, station SANT on the Santorin island in Mediterranian, and some others). Such paths were excluded from the final tomographic inversion.

2) Paths starting from the epicenters at some geographical regions. We noticed only one region, namely the Aegean Sea, which is characterized by significant increase in *Rms* relative to the average values. It could be explained by inconsistent data on source depth and source mechanism specific for this region with complicated lithospheric structure.

3) Paths of different length. The shorter paths (less than 1000 km) and very long paths (>8000 km) are characterized in average by slightly bigger values of *Rms,* but the difference is not very significant.

4) Paths inside some geographical cell. The paths crossing predominantly platforms and shields are characterized by *Rms* values that are lower than these values for paths crossing tectonic regions by a factor of 2 (Figure 11b). This can be explained (at least partly) by inadequacy of our version of the ray theory which does not take into account the effects of focusing and defocusing of wave energy, scattering effects of mountain ranges, and not completely eliminated multipathing. We are inclined to assume that at the existing level of knowledge of the detailed crustal velocity structure in tectonic regions it is practically nonrealistic to improve measurements of short and mid-period surface wave attenuation by introducing more sophisticated theory that takes into account ray bending or frequency-dependent diffraction effects.

CONCLUSIONS

The modified SWAMTOOL technique permits reliable measurement of surface-wave amplitude spectra and the evaluation of the quality of the measurements. We found that the existing networks and the pattern of seismicity provide a significant amount of spectral amplitudes for periods in the range of 14-24 s, appropriate for 2-D tomographic inversions for attenuation coefficients. Data at shorter periods are too scarce for tomographic inversion.

ACKNOWLEDGEMENTS

REFERENCES

Barmin, M. P., M. H. Ritzwoller, and A. L. Levshin (2001). A fast and reliable method for surface wave tomography, *Pure Appl. Geophys*., **158**, 1351-1375.

Bonner, J. L., D. R. Russel, D. G. Harkrider, D. T. Reiter, and R. B. Herrmann (2006). Development of a time-domain, variable-period surface wave magnitude measurement procedure for application at regional and teleseismic distances, *Bull. Seism. Soc. Am*., **96**, 678-696.

Cong, L., and B. J. Mitchell (1998). Lateral variations of Lg coda Q in the Middle East, *Pure Appl. Geophys*., **153**, 563-585.

Cong, L., and B. J. Mitchell (1998a). Seismic velocity and Q structure of the Middle Eastern crust and upper mantle from surface-wave dispersion and attenuation, P*ure Appl. Geophys*., **153**, 503-538.

Dziewonski, A., Chou, T.-A. & Woodhouse, J. H. (1981). Determination of earthquake source parameters From waveform data for studies of global and regional seismicity, *J. Geophys. Res.*, **86**, 2825-2852.

Engdahl, E. R., R. van der Hilst, and R. Buland (1998). Global teleseismic earthquake relocation with Improved travel times and procedures for depth determination. *Bull. Seism. Soc. Am.*, **88**, 722-743.

Jemberie, A.L., and B.J. Mitchell (2004). Shear wave Q structure and its lateral variation in the crust of China and surrounding regions, *Geophys. J. Intl.*, **157**(1), 363-380.

Jemberie, A.L., and B.J. Mitchell (2005). Frequency-dependent shear-wave Q models for the crust of China and surrounding regions, *Pure Appl. Geophys.*, **162**, 21-36.

Keilis-Borok,V.I. (1960) Difference of surface waves spectrum for earthquakes and underground explosions. *Proc. of the Institute of Physics of the Earth, Ac. Sci. USSR*, **15** (182): 88-100 (in Russian).

Levshin, A.L., Pisarenko, V.F., Pogrebinsky, G.A. (1972). On a frequency-time analysis of oscillations, *Ann. Geophys.*, **28**, 211-218.

Levshin, A.L. (1985). Effects of lateral inhomogeneities on surface wave amplitude measurements., *Ann. Geophys.,* **3**, 511-518.

Levshin, A. L., T. B. Yanovskaya, A. V. Lander, B. G. Bukchin, M. P. Barmin, L. I. Ratnikova, and E. N. Its (1989). *Seismic Surface Waves in Laterally Inhomogeneous Earth*. (Ed. V.I. Keilis-Borok), Kluwer Publ. House.

Levshin, A.L., X. Yang, M. H. Ritzwoller, M. P. Barmin, and A. R. Lowry (2006). Toward a Rayleigh Wave attenuation model for Central Asia, in Proceedings of the 28th Seismic Research Review: Ground-Based *Nuclear Explosion Monitoring Technologies*, LA-UR-06-5741, 1-10.

Marshall, P. D. and P. W. Basham (1972). Discrimination between earthquakes and underground explosions employing an improved *Ms* scale, *Geophys. J. R. astr. Soc.*, **28**, 431-458.

Ritzwoller, M. H. and A. L. Levshin (1998). Eurasian surface wave tomography: group velocities, *J. Geophys. Res.*, **103**, 4839-4878.

Russell, D., R. B. Herrman, and H. Hwang (1988). Application of frequency-variable filters to surface wave amplitude analysis, *Bull. Seism. Soc. Am.*, **78**, 339-354.

Russell, D. R. (2006). Development of a time-domain, variable-period surface wave magnitude measurement procedure for application at regional and teleseismic distances, Part I: Theory, *Bull. Seism. Soc. Am.*, **96**, 665-677.

Shapiro, N. M. and M. H. Ritzwoller (2002). Monte-Carlo inversion for a global shear-velocity model of the crust and upper mantle, *Geophys. J. Int.*, **151**, 88-105.

Stevens, J. L., D. A. Adams, and G. E. Baker (2001). Improved surface wave detection and measurement using phase-matched filtering with a global one-degree dispersion model, in *Proceedings of the 23rd Seismic Research Review: Worldwide Monitoring of Nuclear Explosions, LA-UR-01-4454*, Vol. 1, 420-430.

Taylor, S.R., X. Yang, and W.S. Phillips (2003). Bayesian Lg attenuation tomography in Central Asia, *Bull. Seism. Soc. Am.*, **93**, 795-803.

Wessel, P. A. and W. H. Smith (1995). New version of the generic mapping tools released, *EOS, Trans. Amer. geophys. Un.,* **76**, Suppl., 329.

Woodhouse, J. H. (1974). Surface waves in a laterally varying layered structure, *Geophys. J. Roy. Astr. Soc.*, **37**, 461-490.

Yang, X., S. R. Taylor, and H. J. Patton (2004). The 20-s Rayleigh wave attenuation tomography for Central and Southeastern Asia, *J. Geophys. Res.,* **108**, B12304, doi:10.1029/2004JB003193.

Yang, X.A., A. R. Lowry, A. L. Levshin, and M. H. Ritzwoller (2005). Toward a Rayleigh

wave attenuation model for Eurasia and calibrating a new *Ms* formula, in *Proceedings of the 27th Seismic Research Review: Ground-Based Nuclear Explosion Monitoring Technologies,* LA-UR-05-6407, 259-265.
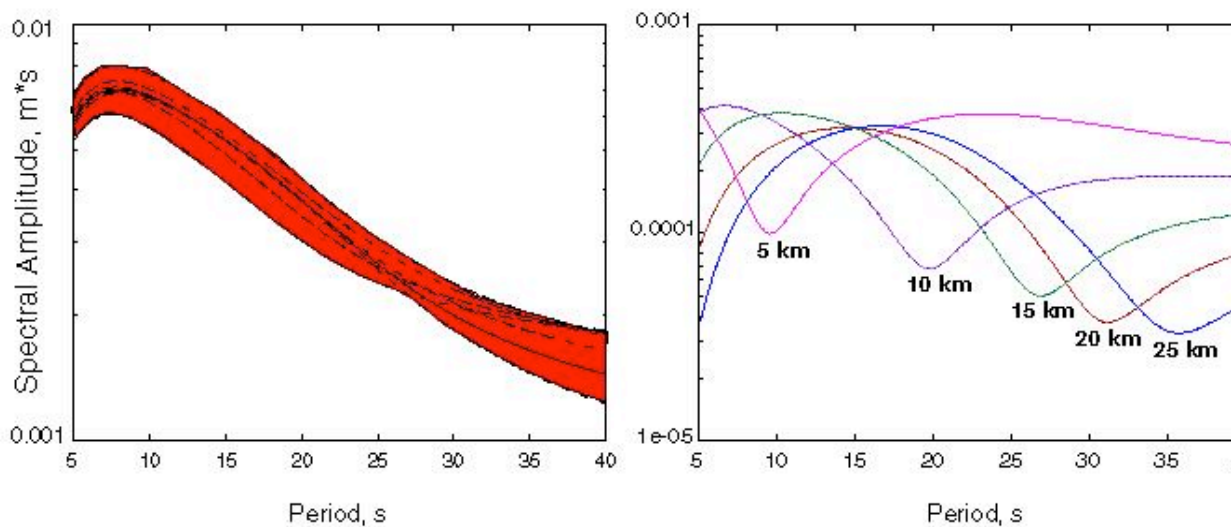
FIGURES

Figure 1. Effects of uncertainties in source parameters for an earthquake in Turkey. Left: the red stripe corresponds to possible range of spectral amplitudes, when strike, dip, and slip determining the best couple vary by ±5°. Parameters of the source: depth= 10 km; dip= 67±5°; rake= -171±5°; difference between strike and the station azimuth is 18±5°. Right: the source depth varies from 5 to 25 km; source parameters are: dip= 70°; rake= -15°, difference between strike and the station azimuth is 144°.
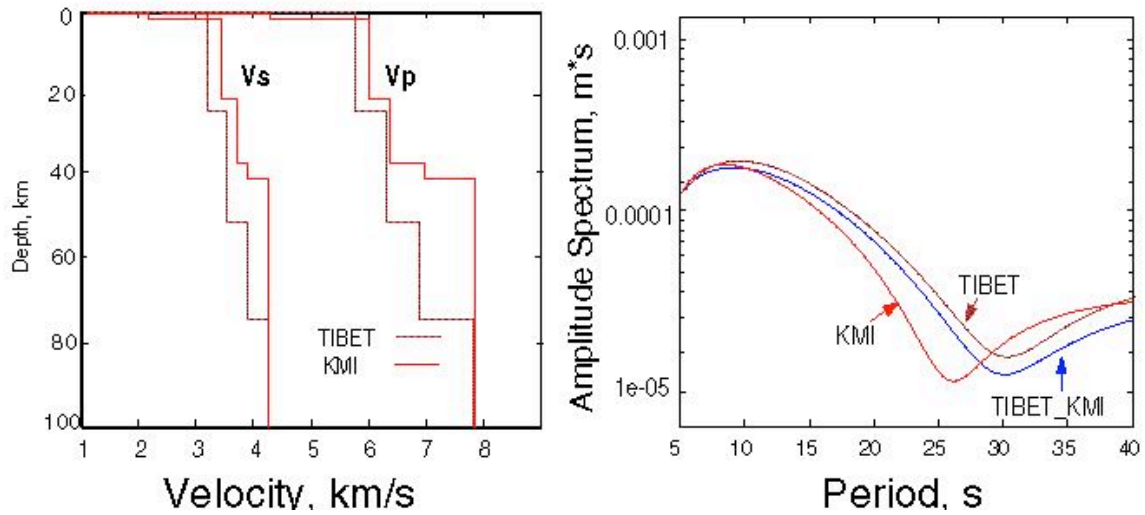
Figure 2. The differences in synthetic amplitude spectra for the path from Tibet to station KMI and a realistic source mechanism. Left: crustal models under the source (TIBET) and receiver (KMI). Right: Synthetic amplitude spectra for three different simulations. TIBET curve is for TIBET model at both event and station locations; KMI curve is for KMI model at both locations; TIBET-KMI curve is for TIBET model near the source and KMI model under the station.
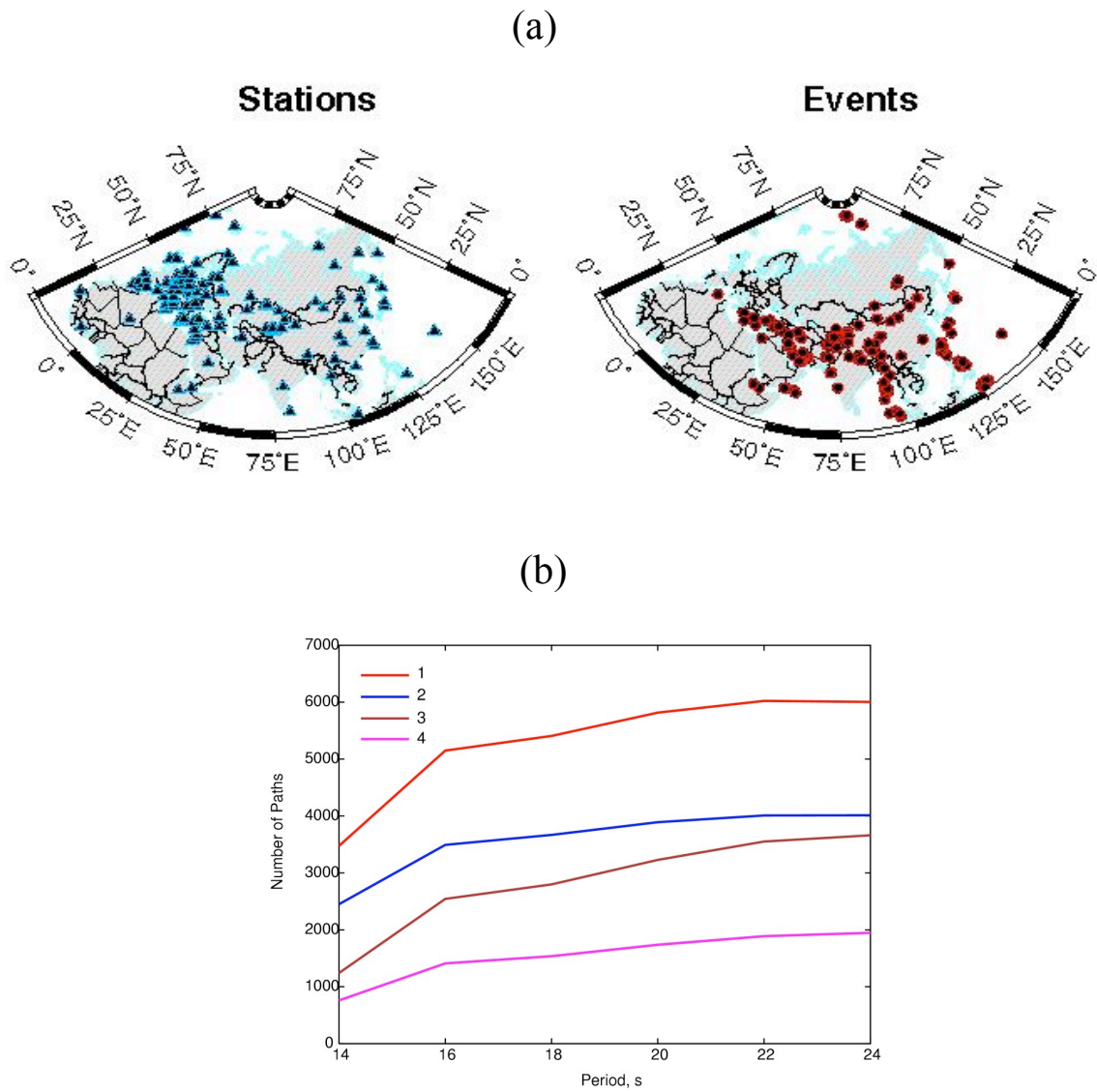
Figure 3. a) Stations and events selected for surface-wave data analysis. **b)** Number of paths for which the spectral amplitudes have been measured: 1-number of raw epicenter-station measurements; 2 - number of epicenter-station paths selected for tomographic inversion; 3- number of raw inter-station measurements; 4 number of inter-station paths selected for validation of tomographic maps.
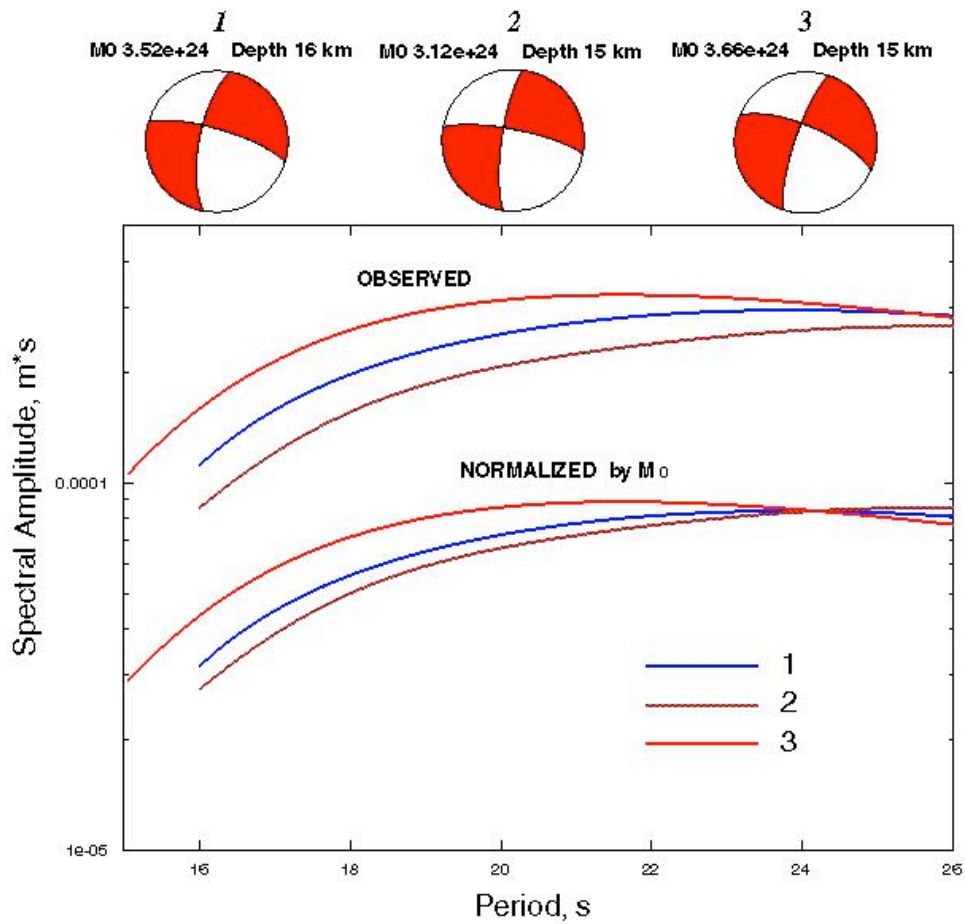
Figure 4. Similarity of amplitude spectra from three closely-located local events in Turkey.
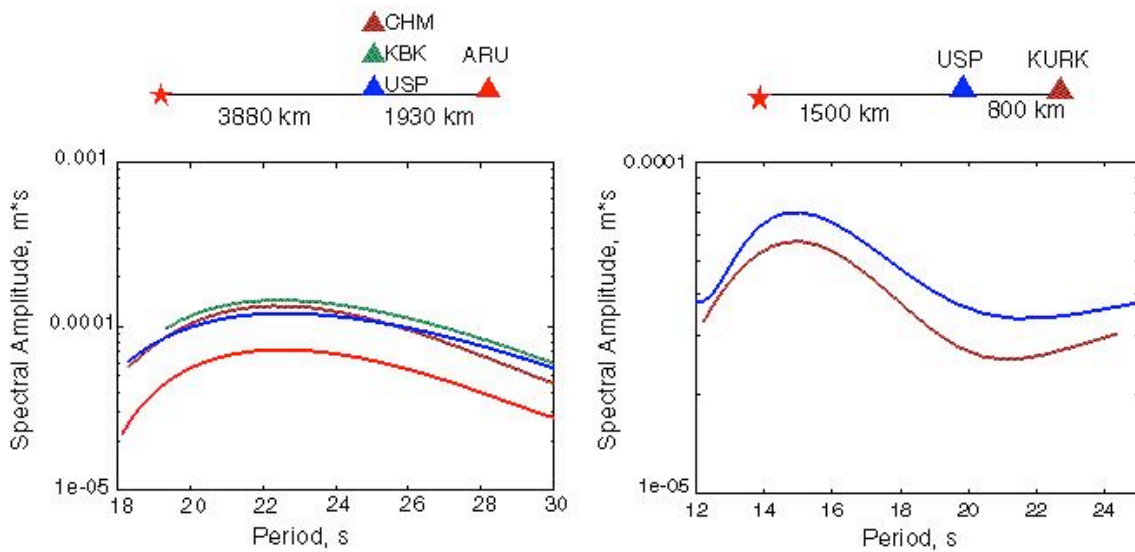
Figure 5. Examples of inter-station measurements by stations of KAZNET and KNET networks. Left: Event near Andaman Islands; Right: Event in Pakistan.
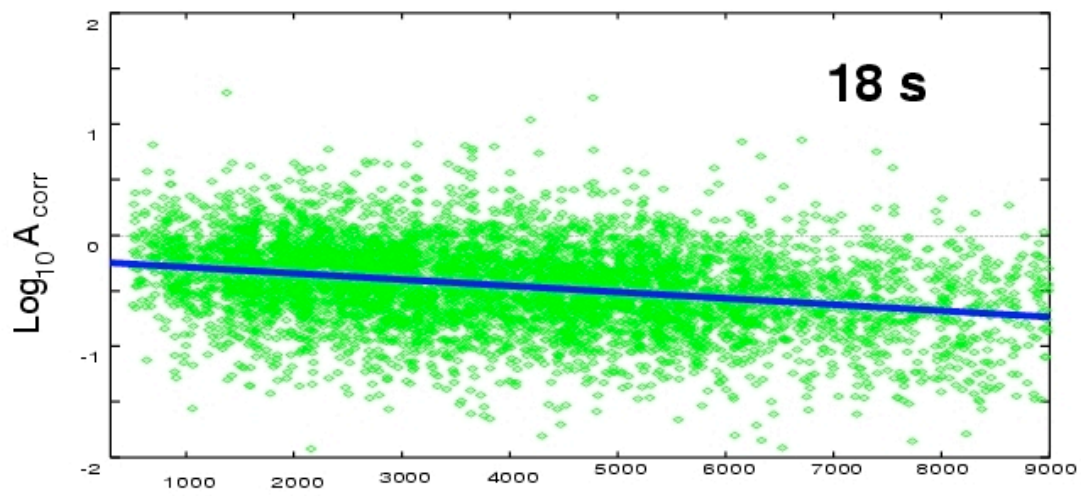
Figure 6. Corrected epicenter-station spectral amplitudes as a function of epicentral distance for 18 s period. Regression line is also shown.
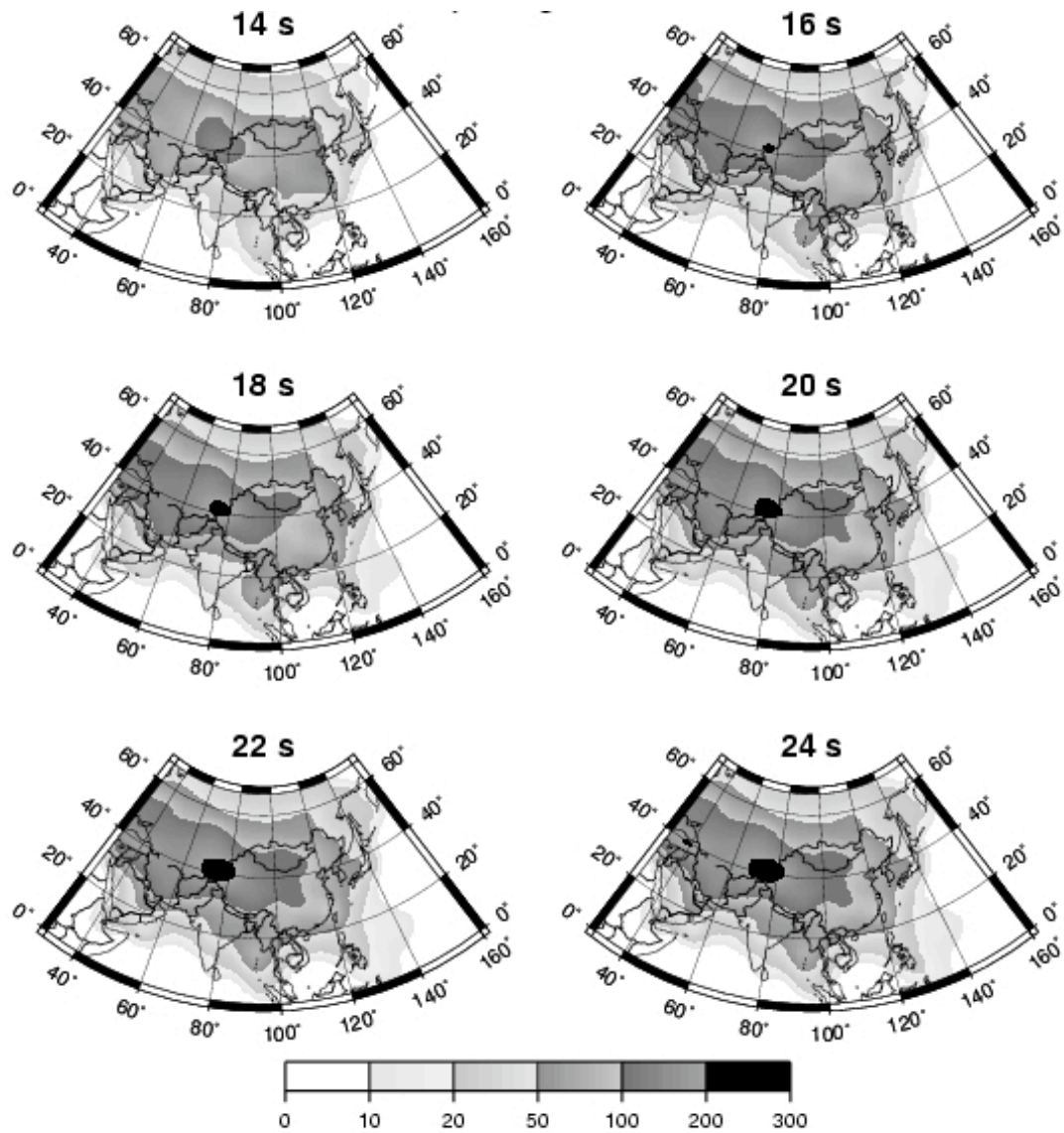
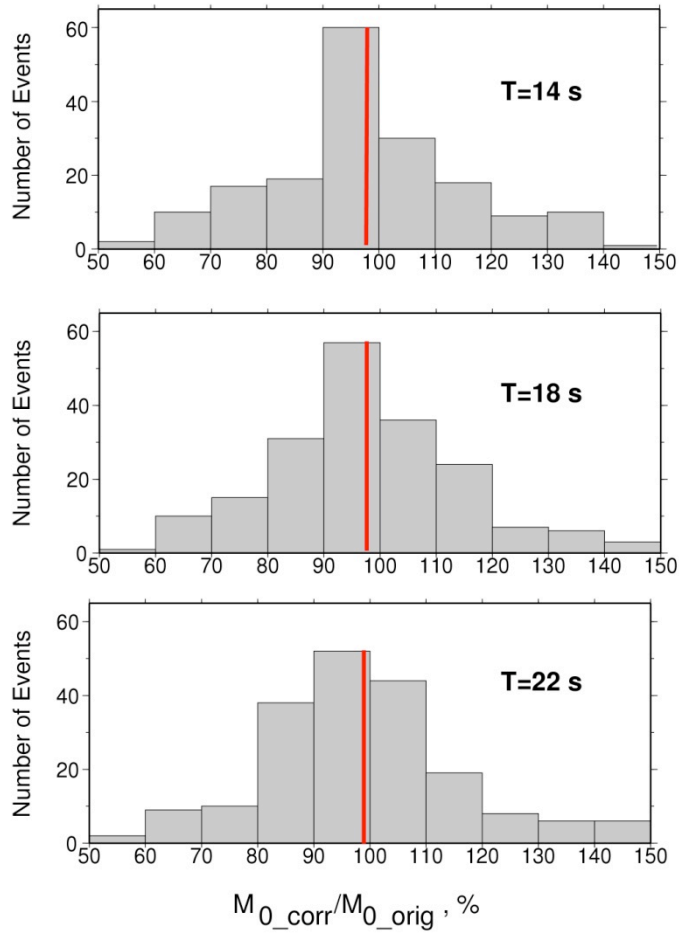**Figure 7.** Path density for selected epicenter-station paths at indicated periods.

Figure 8. Histograms of the ratio M_{0corr} / M_{0CMT} (%) for indicated periods. Red dash line corresponds to an average value of M_0 for a given period. Corrected values of M_0 at 18 s were used to correct attenuation measurements in tomographic inversion for the full set of periods.
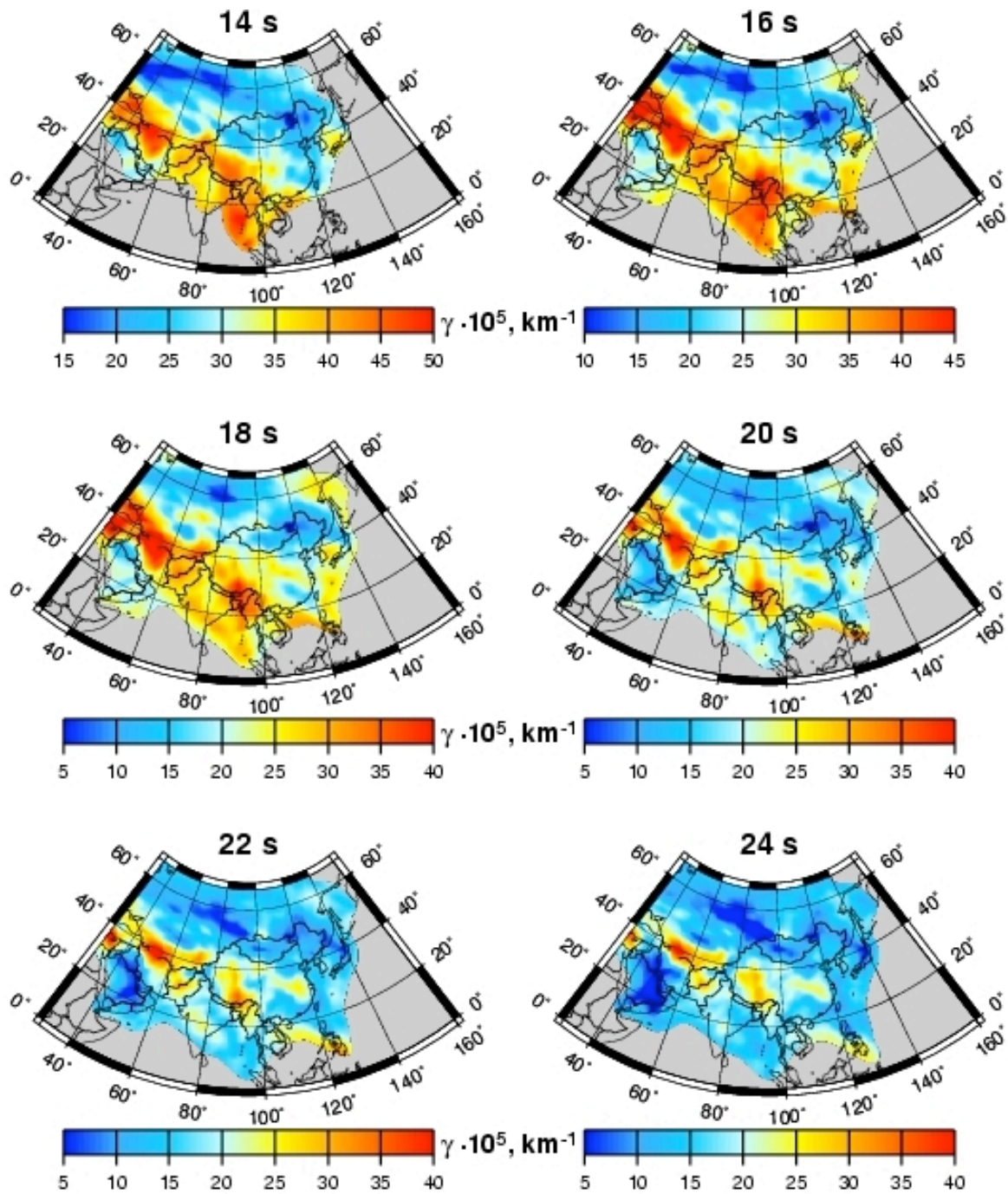
Figure 9. Tomographic maps of attenuation coefficients across Asia and surrounding regions. Grey color corresponds to areas where the path density is less than 20 paths across a 2° by 2° equatorial cell.
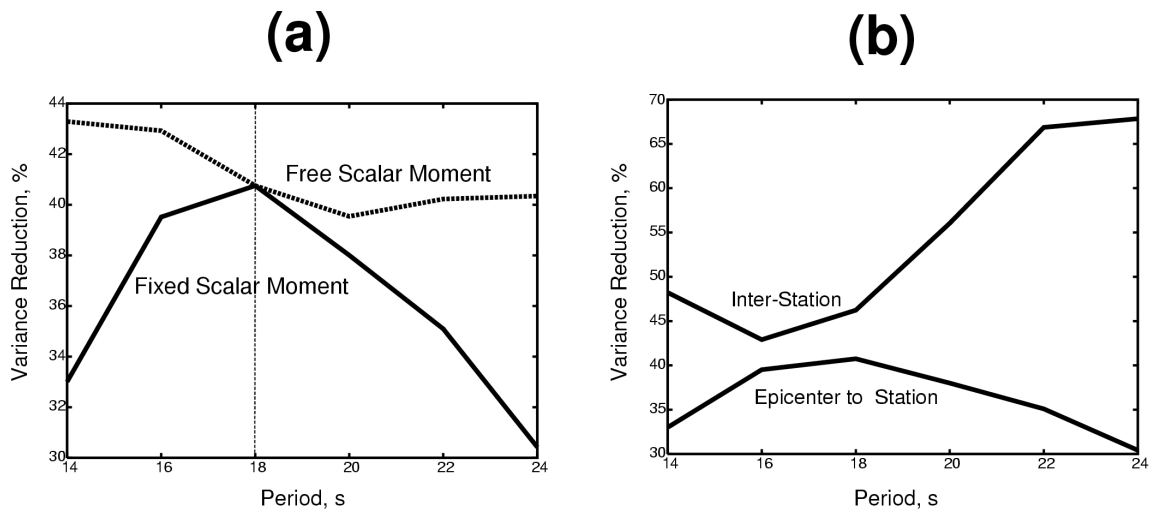
(a)

(b)

Figure 10. a) Variance reduction resulting from the tomographic inversion with "free" scalar moment corrections and from the inversion with fixed corrections according to the results of *T*=18s inversion. b) Resulting variance reductions for epicenter-station and inter-station measurements.
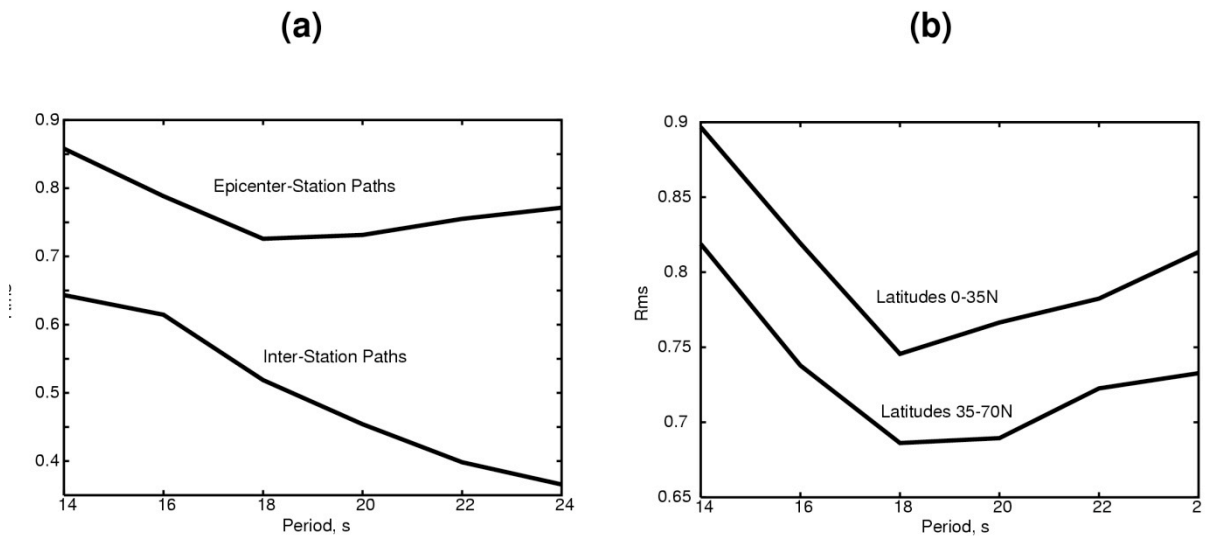

(a)

(b)

Figure 11. a) Average *Rms* values of residuals d_{ij} for the Epicenter-Station and Inter-Station paths. b) Difference in average *Rms* values of residuals d_{ij} for paths crossing platforms and shields (between latitudes 35-70ºN) and tectonic regions (between latitudes 0-35º N).